Journal of Materials Chemistry B

Accepted Manuscript

ROYAL SOCIETY OF CHEMISTRY

www.rsc.org/materialsB

Journal of Materials Chemistry B

Dynamic Article Links ►

Cite this: DOI: 10.1039/c0xx00000x

www.rsc.org/xxxxxx

FULLPAPER

Facile non-hydrothermal synthesis of oligosaccharides coated sub-5 nm magnetic iron oxide nanoparticles with dual MRI contrast enhancement effect

Jing Huang,[a] Liya Wang,[a] Xiaodong Zhong,[b] Yuancheng Li,[a] Lily Yang,[c] Hui Mao [a]*

Received (in XXX, XXX) Xth XXXXXXXXX 20XX, Accepted Xth XXXXXXXXX 20XX
DOI: 10.1039/b000000x

Ultrafine sub-5 nm magnetic iron oxide nanoparticles coated with oligosaccharides (SIO) with dual T_1-T_2 weighted contrast enhancing effect and fast clearance has been developed as magnetic resonance imaging (MRI) contrast agent. Excellent water solubility, biocompatibility and high stability of such sub-5 nm SIO nanoparticles were achieved by using the "*in-situ* polymerization" coating method, which enables glucose forming oligosaccharides directly on the surface of hydrophobic iron oxide nanocrystals. Reported ultrafine SIO nanoparticles exhibit a longitudinal relaxivity (r_1) of 4.1 $mM^{-1}s^{-1}$ and a r_1/r_2 ratio of 0.25 at 3 T (clinical field strength), rendering improved T_1 or "brighter" contrast enhancement in T_1-weighted MRI in addition to typical T_2 or "darkening" contrast of conventional iron oxide nanoparticles. Such dual contrast effect can be demonstrated in liver imaging with T_2 "darkening" contrast in the liver parenchyma but T_1 "bright" contrast in the hepatic vasculature. More importantly, this new class of ultrafine sub-5 nm iron oxide nanoparticles showed much faster body clearance than those with larger sizes, promising better safety for clinical applications.

1. Introduction

Iron oxide nanoparticles (IONPs), also known as superparamagnetic iron oxide (SPIO) nanoparticles, have been extensively investigated as magnetic resonance imaging (MRI) contrast agents in both clinical applications (*e.g.* liver, lymph nodes imaging) and preclinical investigations with animal models (*e.g.* cell tracking and biomarker targeted molecular imaging).[1-4] Typical IONPs predominantly increase the transverse relaxation rate (R_2 or $1/T_2$), together with signal dephasing caused by the perturbed local field, leading to signal drops in T_2 or T_2* weighted MR imaging. However, T_2 or T_2* -weighted MRI with IONPs are often interfered by image artefact and co-found T_2 effects from other signal sources.[5, 6] Therefore, using "bright" T_1 contrast agents that increase longitudinal relaxation rate (R_1 or $1/T_1$) and enhance signal intensity is more desirable for easier and better detection of abnormalities. Early studies have shown that the longitudinal r_1 and transverse r_2 relaxivities of IONPs are dependent on the particle size and the surface coating properties.[7-11] It is conceivable that r_1 relaxivity can be preserved for the ultrasmall IONPs with a core size below 5 nm, due to their relatively lower r_2 relaxivity and larger surface area, which allows more water molecules exchanging between inner and outer layers of particle surface.

To date, various forms of IONPs have been developed for MRI applications, of which only two agents (Feridex®, Resovist®) formulated with dextran coating have been approved by FDA for clinical uses.[12] Both have an average core size over 5 nm and overall size of 60-150 nm.[5, 13] Particles with such overall size are rapidly trapped in the organs of the retoculoendothelia system (RES) and can take several weeks or even months to be degraded and cleared from the body.[14] Slow clearance not only causes concern about long term side effects of such IONPs but also limits them from being used repeatedly in longitudinal imaging studies. Moreover, the larger overall size prevents IONPs from maintaining T_1 contrast enhancement properties.[15, 16]

In order to make IONPs below 5 nm, especially monodispersed IONPs with controlled sizes because of their size-sensitive magnetic properties,[17-20] thermal decomposition is the preferred method. However, the subsequent surface modification to transfer and stabilize IONPs into aqueous physiological conditions is a critical procedure for IONPs applied in diagnostic imaging. Previous reports have shown that the relaxivities that determine MRI contrast enhancement are dependent on the surface properties of IONP-based contrast agents, such as the thickness, the hydrophillity, and the anchoring groups of the coating layer.[21-24] Especially for IONPs below 5 nm, their strong tendency to aggregate makes them difficult to be stabilized in the aqueous media. Traditional surface coating with polymers of high molecular weight, *e.g.* dextran, polyethylene glycol (PEG), poly(methacrylic acid) (PMAA),[25-28] is not effective in stabilizing sub-5 nm IONPs as they are "patchy" and less uniform with tangling chains and inter-molecular steric repulsion. The imperfect surface coating may lead to instability and loss of magnetism, while the subsequent formation of IONP clusters results in the loss of T_1-contrast enhancement properties. Therefore, a new surface modification strategy is needed to ensure the water solubility and stability of IONPs smaller than 5 nm, and to preserve the T_1-weighting contrast effect.

Here we report a new class of ultrafine oligosaccharide coated iron oxide nanoparticles (SIO-3, average core size of 3.5 nm) prepared by *in-situ* polymerization of glucose on the particle surface. The reported sub-5 nm SIO-3 is highly stable in the aqueous solution and exhibits improved r_1/r_2 ratio over IONPs with larger overall sizes, leading to the excellent T_1 MRI contrast enhancement and novel dual T_1-T_2 contrast effect for new applications. In addition, SIO-3 showed shortened body clearance time with partial renal secretion compared with IONPs with larger sizes, therefore, promises to address the lasting concern of possible long term toxicity associated with IONPs.

2. Experimental section

Synthesis of Hydrophobic Iron Oxide Nanoparticles (IONPs). The hydrophobic iron oxide nanoparticles were synthesized by thermo-decomposition. Briefly, iron(III) oleate was first prepared by a modified published method.[20] Typically, 4.04 g of ferric nitride (10 mmol) and 9.13 g of sodium oleate (30 mmol) was dissolved in the solvent mixed with 40 mL distilled water, 50 mL hexane and 10 mL absolute ethanol. The mixture of iron oleate was stirred at room temperature for 4 hours, and then kept still overnight. The resulting red-brownish hexane layer was used as the iron source for thermo-decomposition. In a typical reaction, 5 mL of the iron oleate was mixed with 5 mL of 1-octadecene at room temperature, and degassed with ultrahigh argon for 20 min. After evaporating hexane at 70 °C, the reaction mixture was heated to 320 °C with a heating rate of $0.6\ °C \cdot s^{-1}$. The reaction time was adjusted to control the size of IONPs, which was about 5 min for IONPs with a core size of 3.5 nm, and reheated approximate 10, 15, 20, 30 min for IONPs with 4.8, 9.9, 15.6, 19.9 nm core size. After cooling down to room temperature, ethanol was added to precipitate the nanoparticles. The products were collected by centrifugation, and washed with hexane and ethanol for several times.

Synthesis of Oligosaccharide Coated Iron Oxide (SIO) Nanoparticles. Oligosaccharide coating was introduced on the hydrophobic IONPs by *in situ*-polymerization. Briefly, the oleic acid coated IONPs were redispersed in chloroform after purified with centrifugation, and carefully added dropwise into the preheated glucose solution in dimethylformamide (DMF). The mixture was heated to 120 °C, and kept at this temperature for 2.5 hours. After cooling down to room temperature, the product was precipitated by adding ethanol. The precipitant was washed and centrifuged several times. The final product was collected and redispersed in distilled water for other characterization and applications.

Characterizations of SIO Nanoparticles. The morphology and size of SIO nanoparticles were studied using transmission electron microscope (TEM, Hitachi H-7500, accelerating voltage 75 kV). Typically, TEM samples are prepared by dropping diluted nanoparticle solutions on the carbon coated copper grid and air-dried. The hydrodynamic size and surface charges of nanoparticles in the aqueous solution were evaluated using a dynamic light scattering (DLS) instrument (Malvern Zeta Sizer Nano S-90) equipped with a 22 mW He-Ne laser operating at 632.8 nm. The structural analysis of SIO nanoparticles was carried out by powder X-ray diffraction (XRD, Bruker D8 DIFFRAC powder diffractometer, Co Kα). For studying the nanoparticles coating, Fourier transform infrared spectroscopy (FTIR) spectra were collected on a PerkinElmer Spectrum 100 FT-IR spectrometer (Bucks, UK). UV-vis absorption spectra were obtained with a scanning spectrophotometer (Shimadzu UV-2401PC) with a slit width of 1.0 nm.

Measurement of Relaxation Times and Calculation of Relaxivities. To evaluate MRI contrast enhance capability, SIO solutions with different concentrations were examined with a 3T MRI scanner (Magnetom Tim Trio, Siemens Medical Solutions, Erlangen, Germany) using T_1- and T_2-weighted fast spin echo sequences, inversion recovery turbo spin echo sequence and multi-echo T_2-weighted spin echo sequence. Commercial T_1 enhancement contrast agent Multihance® (Gd-BOPTA) was used for comparing the MRI contrast enhancement effect. Each sample was prepared with Fe or Gd concentrations varying from 0.004 to 40 mM. To measure the longitudinal relaxation time T_1, an inversion recovery turbo spin echo (TSE) sequence with echo train length (ETL) of 3, echo time (TE) of 13 ms and repetition time (TR) of 1500 ms was used to obtain images at different inversion times (TI) of 23, 46, 92, 184, 368, 650, 850, 1100, and 1400 ms, respectively. To measure the transverse relaxation time T_2, a multi-echo spin echo sequence was used with TR of 2400 ms and 15 TEs, starting at 11 ms with increments of 11 ms. Signal intensity (SI) of each region-of-interest (ROI) at different TI or TEs was measured for samples of each concentration.

MRI of Mice Administered with SIO Nanoparticles. All animal experiments were conducted following a protocol approved by Institutional Animal Care and Use Committee (IACUC). BALB/c mice were anesthetized by intraperitoneal injection of a ketamine-xylazine mixture (95:5 mg/kg). The saline diluted SIO-3 solution was intravenously administered at a dosage of 2.5 and 10 mg Fe per kg of mouse body weight. For comparison, Gd-BOPTA and SIO-20 (core size of 20 nm) were injected at the dosage of 2.5 mg/kg and 0.2 mmol/kg, respectively. Fat suppressed T_1-weighted spin echo images were obtained to investigate the contrast changes in different organs and anatomic structures, such as liver, kidney and iliac artery, at the different time points. The imaging parameters included: TR) = 724 ms, TE =10 ms, matrix = 320×134, field of view (FOV) = $120 \times 60\ mm^2$, flip angle = 70, and slice thickness = 1.00 mm. The signal-to-noise ratio (SNR) was calculated according to the equation: $SNR = SI_{mean}/SD_{noise}$. The relative contrast enhancement at different time points was defined as signal decrease $\Delta SNR = (SNR_{pre}-SNR_{post})/SNR_{pre.}$ The contrast-to-noise ratio between liver parenchyma and vasculature was calculated as $CNR = (SNR_{post(vasculature)}-SNR_{post(liver\ parenchyma)})/SNR_{pre(liver\ parenchyma)}$.

Body Clearance of SIO Nanoparticles in Mice. The clearance of nanoparticles were evaluated by both chemical analysis of iron contents from the collected organs tissues and ROI analysis of T_2-weighted MRI and T_2 relaxometry mapping of live animals, which allows for time dependent changes of iron concentrations at the specific organ in the same animal. SIO-3, SIO-20 and SHP20, which is commercial available amphiphilc polymer coated SPIO (core size 20 nm from Ocean NanoTech, LLC), were intravenously administered into BALB/c mice (n= 3) at a dosage of 2.5 mg/kg mouse weight. For MRI monitoring, T_2-weighted MR images of the mice were acquired on a 3 T MRI scanner before and after administration of nanoparticle contrast agents using a volumetric wrist coil. The imaging parameters included: TR = 3710 ms, TE =12-180 ms, matrix = 256 × 128, field of view (FOV) = 120 × 60 mm^2, flip angle = 180°, and slice thickness = 1 mm. Colorized T_2 maps were then generated as described in the supporting information. ROIs with the same areas were drawn in the liver and spleen at the same T_2 maps. The relative contrast enhancement at different time points was calculated to show the average signal changes. The organs (liver, spleen, kidney, lung, heart, and muscle) and blood samples were collected at 10 min, 1 day, 1 week, 2 weeks and 3 weeks after injection. For chemical analysis of tissue iron, phenanthroline colorimetric method was used to determine the iron concentration in organs after the organs were digested in concentrated HNO_3.[29] In addition, Prussian blue staining was performed for the major organ slices following a standard protocol. Briefly, frozen tissues mounted in optimal cutting temperature compound (OCT) were sliced in 8 μm thickness, fixed with 4% paraformalin for 10 min, then soaked into working solution composed of 10% potassium ferrocyanide (II) trihydrate and 20% HCl solution (v:v = 1: 1) at 37 °C for 4 hours. After washed with PBS, slices were counterstained with nuclear fast red for 5 min. Blue dots represents the remained IONPs in organs were investigated with a light microscope.

3. Results and discussion

IONPs with different diameters were prepared by thermal decomposition of ferric oleate through adjusting decomposition conditions. The hydrophobic IONPs were highly uniform with diameters of 3.5 (IO-3), 4.8 (IO-5), 9.9 (IO-10), 15.6 (IO-15), and 19.9 nm (IO-20) respectively, as revealed TEM images (Figure 1 and Figure S1). In this work, the hydrophobic IO nanoparticles were mixed with glucose solution in DMF, and heated to allow the *in situ*-polymerization of glucose on the particle surface. A thin oligosaccharides coating layer was formed, rendering water soluble nanoparticles. The core sizes showed no significant changes before and after the surface modification (Figure 1c, Figure S1e-h). To evaluate the hydrodynamic diameters of these oligosaccharides coated IONPs in aqueous solution, DLS measurement were performed. The hydrodynamic sizes are 7.3, 9.5, 11.5, 15.7, 20.9 nm for SIO-3, 5, 10, 15, 20, respectively (Figure S2), which are slightly larger than the TEM core sizes due to the addition of the hydrophilic oligosaccharide coating layers. The hydrodynamic size of 7.3-nm measured in SIO-3 suggests the thinnest coating layer among those IONPs with core size below 5 nm, which may play the significant role in preserving the T_1 contrast enhancing effect due to less restraints in water exchange between inner and outer layers.[21, 24, 27, 28, 30] Moreover, the small hydrodynamic size indicates the single dispersion of SIO-3 in the aqueous solution, preventing the T_2 effect caused by the aggregation.[23] The oligosaccharide coated particles were stable and highly dispersed in the aqueous solution at room temperature for at least 2 months, showing no aggregation (Figure S3).

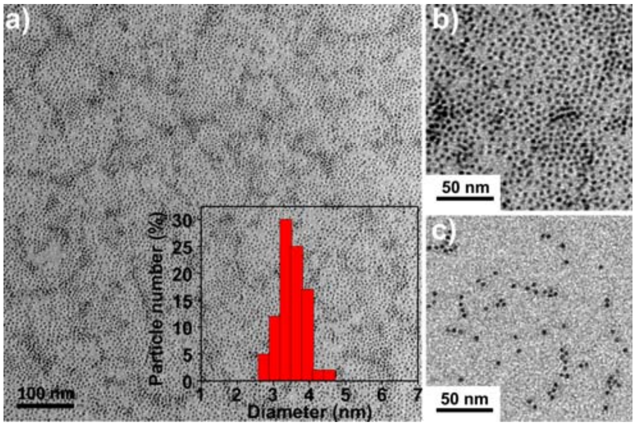

Figure 1. (a) A low magnification and (b) high magnification TEM images of hydrophobic IONPs sized in 3.5 nm (IO-3). The inset of (a) is the size distribution after measured 100 particles. (c) TEM images of hydrophilic IONPs coated with oligosaccharides (SIO-3).

The powder X-ray diffraction (XRD) patterns of IO-3 and SIO-3 were shown in Figure 2a. Broadened diffraction peaks were observed for both samples due to the ultrfine nano-sized crystals. The broadened diffraction peaks became clearer after the coating applied, due to the rearrangement of the canted surface during the heating process.[31] However, the grain size changed little according to the half width of the diffraction peaks. Both of the XRD peaks of IONPs before and after coating were assigned to the spinal magnetite or maghemite structure. The formation of oligosaccharides coating on the surface of IONPs was further confirmed by Fourier-Transform infrared spectroscopy (FTIR) (Figure 2b). The characteristic bands of oleic acid, including C-H stretching (2923, 2852 cm^{-1}), CH_2 bending (1457, 1375 cm^{-1}) and C=O stretching (1540 cm^{-1}), became weakened after being replaced by oligosaccharides on the surface. The emerged sharp C=C band at 1653 cm^{-1} indicated the presence of aromatic structures from oligosaccharides on the particle surface.[32, 33]

It should be noted that the temperature we used to in-situ polymerize glucose on the surface of nanoparticles is much lower (~120 °C) than the established hydrothermal methods used to synthesize carbonized materials from glucose.[32, 34-36] When the formation of oligosaccharides was monitored by UV and fluorescent spectroscopy, a turquoise fluorescent signal with UV excitation at λ=365 nm was observed (Figure 2c) after 0.5 h reaction. This signal can be ascribed to the aromatic groups derived from the intermolecular dehydration and aldol condensation during glycosylation.[32, 35, 36] At this time, oleic acid capped IONPs began to transfer into the aqueous phase as the formation of oligosaccharides coating took place. However, at this early stage, the hydrophillic oligosaccharides were insufficient to stabilize the particles in the aqueous solution, resulted in a light yellow turbid dispersion (Figure 2d). In order to keep the small size of the whole particle, oligosaccharide coating was controlled to be minimal, but sufficient to stabilize the particles. When the IONPs were well transferred and dispersed into aqueous solution (i.e. reaction time is 2.0 h, yielded brownish transparent solution), the reaction was terminated immediately. Parallel experiments indicated the pivotal role of DMF solvent in the formation of oligosaccharide coating, together with the possible catalytic effect from cationic iron.[37] DMF provides an alkaline condition for the glycosylation and facilitates the reaction by absorbing water molecules produced during the polymerization.[38] Evidently, glycosylation under the same reaction conditions, but in different solvents, *e.g.,* octadecene (ODE), diethylene glycol (DEG), and dimethyl sulfoxide (DMSO), did not yield such sufficient oligosaccharides (Figure S4).

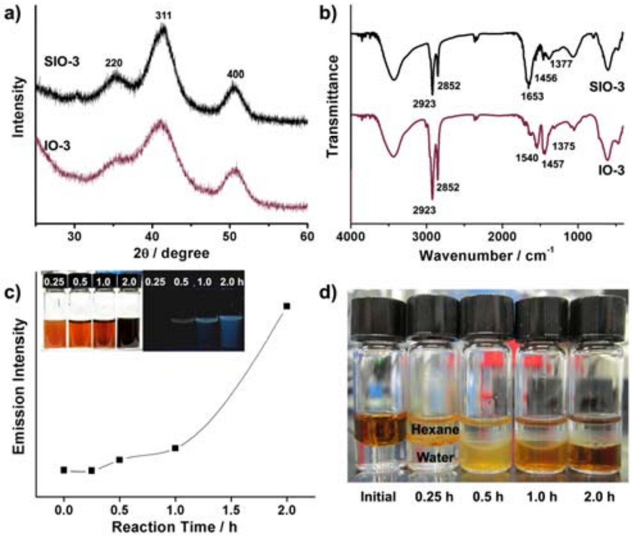

Figure 2. (a) Powder XRD pattern and (b) FTIR spectra of IO-3 and SIO-3. (c) Monitoring of reaction stage by FL emission. The inset of (c) is photographs of the reaction mixture collected at different reaction time under normal light (left) and 365 nm UV light (right). (d) Solvent phase transition of IONPs from organic phase hexane to the aqueous solution over time.

The MRI contrast enhancement effects of SIOs were investigated at the clinically relevant magnetic field (3 T). Figure 3a and b shows T_1- and T_2-weighted MR images of the SIO aqueous solutions with different Fe concentrations. SIO-3 exhibits the highest T_1 contrast enhancement, while SIO-20 exhibits the highest T_2 contrast enhancement. This observation is expected, as SIO-3 has the highest surface-to-volume ratio due to the ultrafine size. For the nanoparticulate contrast agents, the T_1 contrast enhancement is believed to be majorly contributed by the inner-sphere relaxivity, which comes from the direct coordination between water molecules and magnetic ions on the particle surface.[5, 27, 39] High surface-to-volume ratio in combination thin hydrated coating layer of oligosaccharides for SIO-3 would facilitate water molecules interact with the inner layer.

Although transverse relaxivity r_2 of IONPs have been extensively studied,[19] and could be predicted theoretically, limited analysis was done with longitudinal relaxivities r_1 of IONPs. Size, coating, crystallinity, and composition of nanoparticle cores are considered to be important factors in maintaining T_1 effect, according to the Solomon–Bloembergen–Morgan (SBM) theory.[40] It's well recognized that both r_1 and r_2 increase with the increased size however with different proportions, as r_2 has a stronger size dependent effect than r_1.[10] In our case, both r_1 and r_2 of SIO showed size dependency (Figure 3c, d). The increased r_2 with increased size could be ascribed to the size dependent magnetic susceptibility (Figure S5). On the other hand, r_1 of SIOs kept rising until reached a maximum around 10 nm-sized. The similar trends were observed for the ultrasmall IONPs coated with PEG, CTAB, DEG.[10, 19, 41, 42] Such size dependency on r_1 is attributed to the monodispersed size, together with the compact and highly hydrophilic coating, resulted in the good dispersity in solvent without the aggregation. For the larger particles (>10 nm), longitudinal relaxivity r_1 decreased with the increased size, which is attributed to the locked particle magnetic moment on anisotropy axes, thus relaxivity is dominated by Curie relaxation.[19, 43]

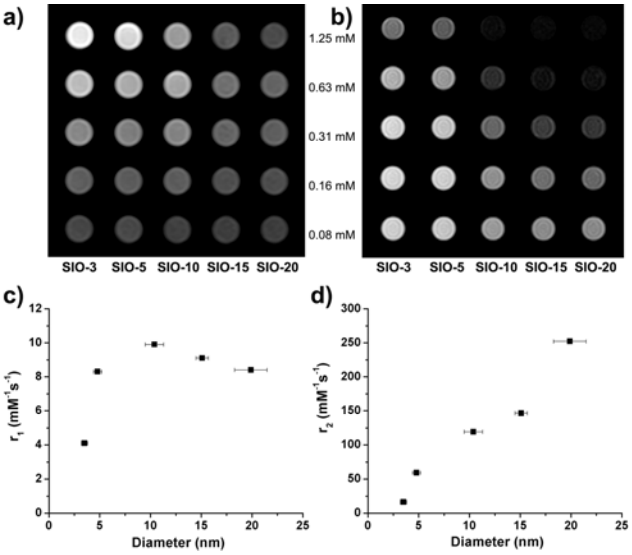

Figure 3. (a) T_1- and (b) T_2-weighted MR images of SIO solutions with different concentrations, and the corresponding (c) r_1 and d) r_2 value changes with particle size.

To further evaluate the contrast enhancement efficiency and behaviour of SIOs, we computed a signal intensity profile of a contrast agent (Figure 4a, b) using the equation describing signal intensity (SI) evolution from the T_1-weighted spin echo sequence. Given the same Fe concentration (*i.e.*, 1 mM) and image acquisition parameters (*i.e.*, TR=500 ms, TE=12 ms) typically used for T_1-weighted spin echo MRI, the highest T_1 contrast, *i.e.*, brightest signal, for a given r_1 can be only obtained when r_2 reaches zero. Furthermore, SI is more sensitive to the change in r_2 than in r_1 for the contrast agents with an r_1 larger than 4.5 $mM^{-1}s^{-1}$. For example, although SIO-3 has a lower r_1, it has a much higher T_1 enhancement efficiency than SIO-20 because of a sharper reduction in r_2.

Early studies have suggested that the r_1/r_2 ratio may dictate the T_1 contrast enhancement properties of the magnetic nanoprobes.[5, 16] An increased maximum SI in T_1-weighted MR images was observed with the increasing r_1/r_2 ratio as shown in Figure 4c. It has been theoretically studied that the r_1/r_2 ratios are monotonically increase against the translational diffusion time τ_D,[24] which is related to the radius of IONPs, water permeability of the coating layer and the coating thickness. Unsurprisingly, SIO-3 has the highest r_1/r_2 ratio of 0.25 comparing to the counterparts in different sizes (Figure 4d).

Since most nanoparticulate T_1 contrast agents reported so far have an r_1 larger than 4.5 $mM^{-1}\cdot s^{-1}$ but also substantially high r_2,[16] one alternative strategy for future development of magnetic nanoparticle based T_1-weighted MRI contrast agents is to attenuate r_2 while attempting to increase r_1. For example, magnetic cation with unpaired electrons (*e.g.* Mn^{2+}, Gd^{3+}) have been introduced into iron oxide nanostructures to increase r_1, thus to realize the positive contrast enhancement.[6, 42, 44] Regardless of the metal toxicity, Gd-doping may be considered as more effective way because of the slighter increase of r_2.[6] Moreover, reducing r_2 may allow an increasing IONP concentration for the T_1 SI enhancement, which is often compromised at the higher IONP concentrations.

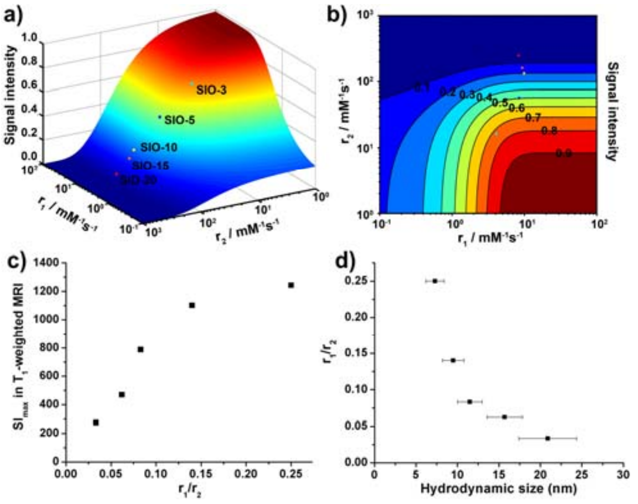

Figure 4. (a) Prediction of SI in T_1-weighted MR images determined by r_1 and r_2, and (b) the top view. (c) The maximum SI of each SIO solutions related to the r_1/r_2 ratio. (d) r_1/r_2 ratio changes with hydrodynamic sizes.

With good biocompatibilities (i.e. non-toxic to cells up to 200 μg/mL, Figure S6), the T_1 contrast enhancement of SIO-3 *in vivo* was investigated. MRI was performed on a 3 T MRI scanner for mice intravenously injected contrast agents. SIO-3 showed excellent positive T_1 contrast enhancement in the vasculature and highly vascularised organs, e.g. heart, kidney and spleen (Figure 5 and 6). In comparison, T_1 contrast enhancement is not obvious in the group injected with SIO-20. Interestingly, SIO-3, particularly at the higher dosage (10 mg/kg), led to a “dual” T_1-T_2 contrast effect in the T_1-weighted MR images as shown in the liver (Figure 5). Both “darkening” T_2 contrast in the liver parenchyma and “bright” T_1 contrast in the hepatic vasculature were observed at the same time. The darkening T_2 contrast in liver parenchyma is caused by the uptake of SIO-3 by Kupffer cells which results in a dominant T_2-effect due to the r_2 increase after intracellular clustering of SIO-3.[45] On the other hand, the bright T_1 contrast in the vasculature is attributed to SIO-3 highly dispersed in the blood pool. This “dual” contrast effect of SIO-3 improves the sensitivity and image clarity for visualizing the morphology of the liver parenchyma and structure of hepatic vasculature, which cannot be achieved by either SIO-20 or Gd-BOPTA alone (Figure 6f). Therefore, it potentially provides the capability of circumscribing a liver mass or detection of very small liver lesion with information from both size/volume and tumor vasculature at the same time using only one contrast agent instead of generating “double” contrast by sequentially injections of both IONPs and Gd-DTPA as explored previously.[46, 47]

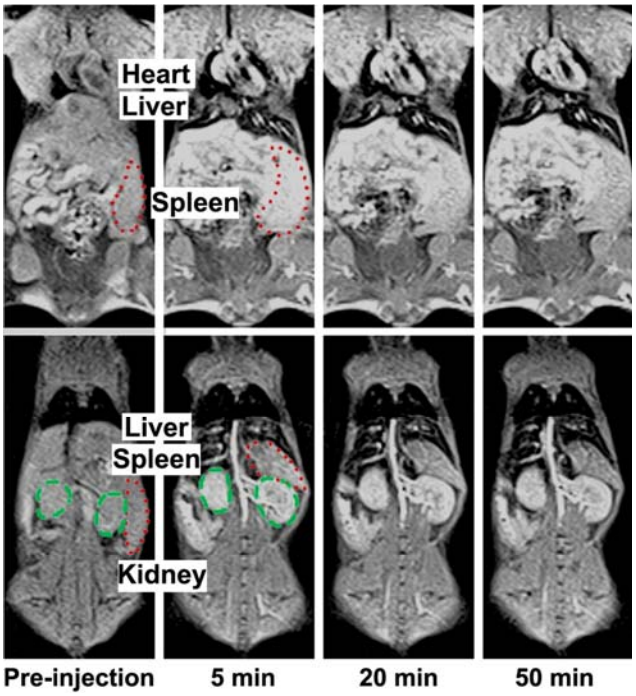

Figure 5. Fat-suppressed T_1-weighted MR images of a mice before and after administration of SIO-3 at a dosage of 10 mg/kg. Positive contrast enhancement were observed in heart, spleen (red dotted circle), kidney (green dashed circle), and liver vessels.

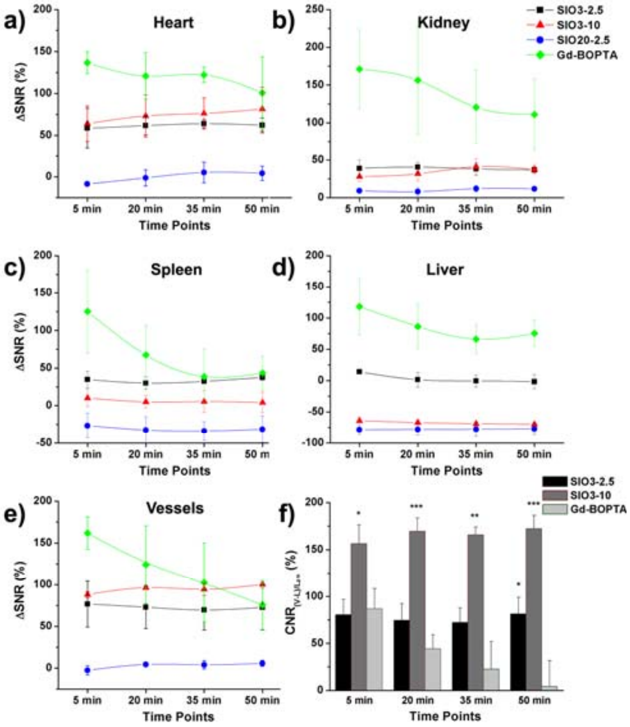

Figure 6. Percentage of signal changes in mouse major organs (n=3) after administration of contrast agents, (a) heart, (b) kidney, (c) spleen, (d) liver, (e) vessels. (f) Contrast changes between liver parenchyma and vessels (n=3); (*P<0.05, **P<0.01, ***P<0.001; t-test).

T_1 contrast enhancement in kidney by SIO-3 may also offer potential applications of imaging renal functions, especially in patients suffering from NSF and who are vulnerable to Gd toxicity. The accumulation of SIO-3 in the kidney, but not SIO-20, suggested possible renal clearance of the sub-5 nm IONPs due to the smaller hydrodynamic size than 8 nm.[48, 49] Both T_1 and T_2-weighted images of mice administrated with SIO-3 showed the gradual changes of MRI signals in the bladder over the time, indicating the excretion of SIO-3 from kidney to the bladder at the time of 1 hour after administration (Figure 7) and the stability of the nanoparticles in blood stream upon filtrated and secreted by the kidney. Such MRI signal changes were not observed in the bladders of those animals receiving larger sized IONPs, such as SIO-20.

To further examine the body clearance of SIO-3 accumulated in RES organs, we used MRI to follow the change of T_2 "darkening" contrast and T_2 relaxometry mapping in the liver and spleen (Figure 8), which was shown to be correlated to the iron concentration in the tissue. The results showed the almost complete recovery of T_2 values of liver and spleen to the pre-injection level in two weeks after injection of SIO-3. However, only 60% was recovered in animals received SIO-20, suggesting a much faster clearance of SIO-3 from the liver. Consistent with *in vivo* MRI observation, the *ex vivo* biodistribution data based on iron concentration analysis also revealed the faster clearance of SIO-3 than SIO-20 in liver and spleen (Figure S7). Furthermore, the oligosaccharide coated IONPs (SIO-20) showed faster clearance in liver and spleen, compared with the conventional bi-block copolymer-coated IONPs (SHP20).

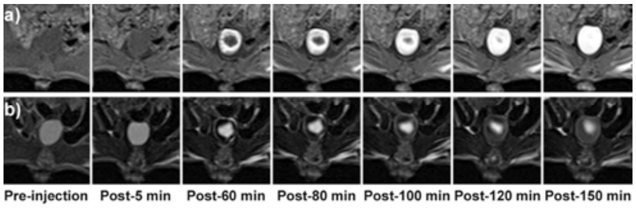

Figure 7. Signal and contrast changes over time in (a) T_1- and (b) T_2-weighted MR images of the bladder of a mouse received SIO-3 reveal the excretion of SIO-3 by kidney. Slow filling SIO-3 into the bladder resulted in slow and gradual extension of the brightening T_1 signal (a) and darkening T_2 signal (b).

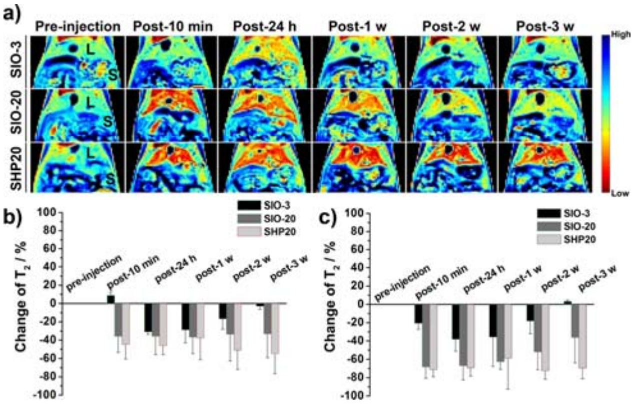

Figure 8. Clearance studies of intravenously administered SIO nanoparticles at 2.5 mg Fe/kg in BALB/c mice. (a) Pseudo colored T_2-maps following the clearance of nanoparticles in liver (L) and spleen (S). The corresponding signal change of (b) liver and (c) spleen in T_2-wiehgted MR images (n =3).

4. Conclusions

In summary, a new class of highly stable and biocompatible oligosaccharides coated sub-5 nm ultrafine IONPs has been developed for improving T_1 contrast enhancement in MRI. The stability of such sub-5 nm SIOs is achieved by *in-situ* polymerization of glucose on the particle surface. The resulting ultrafine SIOs exhibit excellent stability and colloidal properties in physiological medium with improved T_1 MRI contrast enhancing effect, thus providing a potential blood pool MRI contrast agents with longer blood half-time than small molecule contrast agents. Furthermore, dual T_1-T_2 dual contrast observed in liver imaging provides a new capability of simultaneous imaging of liver parenchyma and lesion as well as vasculature using one single agent in clinical applications. More importantly, sub-5 nm SIO showed faster clearance from RES than that of IONPs with the larger size, and can be also secreted from kidney, thus may potentially address the long term toxicity concerns associated with translating such material to clinic imaging.

Notes and references

[a] *Department of Radiology and Imaging Sciences, Emory University School of Medicine, Atlanta, Georgia 30322, USA. Fax: E-mail: hmao@emory.edu*
[b] *MR R&D Collaborations, Siemens Healthcare, Atlanta, Georgia 30322, USA.*
[c] *Department of Surgery, Emory University School of Medicine, Atlanta, Georgia 30322, USA.*

† Electronic Supplementary Information (ESI) available: DOI: 10.1039/b000000x/.

‡ This work is supported in parts by Cancer Nanotechnology Platform Project (CNPP) grant (U01CA151810-02 to HM and LY) and a research grant (R01CA154846-02 to HM and LY) from National Institutes of Health.

1. B. Y. S. Kim, J. T. Rutka and W. C. W. Chan, *New Engl. J. Med.*, 2010, **363**, 2434-2443.
2. A. J. Cole, V. C. Yang and A. E. David, *Trends Biotechnol.*, 2011, **29**, 323-332.
3. E. T. Ahrens and J. W. M. Bulte, *Nat. Rev. Immunol.*, 2013, 755-763.
4. D. Ghosh, Y. Lee, S. Thomas, A. G. Kohli, D. S. Yun, A. M. Belcher and K. A. Kelly, *Nat. Nanotechnol.*, 2012, **7**, 677-682.
5. H. B. Na, I. C. Song and T. Hyeon, *Adv. Mater.*, 2009, **21**, 2133-2148.
6. Z. Zhou, D. Huang, J. Bao, Q. Chen, G. Liu, Z. Chen, X. Chen and J. Gao, *Adv. Mater.*, 2012, **24**, 6223-6228.
7. J. H. Lee, Y. M. Huh, Y. W. Jun, J. W. Seo, J. T. Jang, H. T. Song, S. Kim, E. J. Cho, H. G. Yoon, J.-S. Suh and J. Cheon, *Nat. Med.*, 2007, **13**, 95-99.
8. H. Duan, M. Kuang, X. Wang, Y. A. Wang, H. Mao and S. Nie, *J. Phys. Chem. C*, 2008, **112**, 8127-8131.
9. J. Huang, L. Wang, R. Lin, A. Y. Wang, L. Yang, M. Kuang, W. Qian and H. Mao, *ACS Appl. Mater. Interfaces*, 2013, **5**, 4632-4639.
10. L. Zhang, X. Zhong, L. Wang, H. Chen, Y. A. Wang, J. Yeh, L. Yang and H. Mao, *J. Magn. Reson. Imaging*, 2011, **33**, 194-202.
11. J. Huang, X. Zhong, L. Wang, L. Yang and H. Mao, *Theranostics*, 2012, **2**, 86-102.

12. L. H. Reddy, J. L. Arias, J. Nicolas and P. Couvreur, *Chem. Rev.*, 2012, **112**, 5818-5878.
13. I. Hilger and W. A. Kaiser, *Nanomedicine*, 2012, **7**, 1443-1459.
14. L. Gu, R. H. Fang, M. J. Sailor and J.-H. Park, *ACS Nano*, 2012, **6**, 4947-4954.
15. C. Chambon, O. Clement, A. Leblanche, E. Schoumanclaeys and G. Frija, *Magn. Reson. Imaging*, 1993, **11**, 509-519.
16. S. Laurent, L. V. Elst and R. N. Muller, in *The Chemistry of Contrast Agents in Medical Magnetic Resonance Imaging, Second Edition*, eds. A. Merbach, L. Helm and É. Tóth, John Wiley & Sons, Ltd, Chichester, UK. , 2013.
17. Y. W. Jun, J. W. Seo and A. Cheon, *Acc. Chem. Res.*, 2008, **41**, 179-189.
18. Q. L. Vuong, J. F. Berret, J. Fresnais, Y. Gossuin and O. Sandre, *Adv. Healthcare Mater.*, 2012, **1**, 502-512.
19. E. D. Smolensky, H.-Y. E. Park, Y. Zhou, G. A. Rolla, M. Marjanska, M. Botta and V. C. Pierre, *J. Mater. Chem. B*, 2013, **1**, 2818-2828.
20. J. Park, K. J. An, Y. S. Hwang, J. G. Park, H. J. Noh, J. Y. Kim, J. H. Park, N. M. Hwang and T. Hyeon, *Nat. Mater.*, 2004, **3**, 891-895.
21. U. I. Tromsdorf, O. T. Bruns, S. C. Salmen, U. Beisiegel and H. Weller, *Nano Lett.*, 2009, **9**, 4434-4440.
22. J. Nam, N. Won, J. Bang, H. Jin, J. Park, S. Jung, S. Jung, Y. Park and S. Kim, *Adv. Drug Delivery Rev.*, 2013, **65**, 622-648.
23. A. Roch, R. N. Muller and P. Gillis, *J. Chem. Phys.*, 1999, **110**, 5403-5411.
24. J. Zeng, L. Jing, Y. Hou, M. Jiao, R. Qiao, Q. Jia, C. Liu, F. Fang, H. Lei and M. Gao, *Adv. Mater.*, 2014.
25. K. E. Kellar, D. K. Fujii, W. H. H. Gunther, K. Briley-Saebo, A. Bjornerud, M. Spiller and S. H. Koenig, *J. Magn. Reson. Imaging*, 2000, **11**, 488-494.
26. L. Sandiford, A. Phinikaridou, A. Protti, L. K. Meszaros, X. Cui, Y. Yan, G. Frodsham, P. A. Williamson, N. Gaddum, R. M. Botnar, P. J. Blower, M. A. Green and R. T. M. de Rosales, *ACS Nano*, 2013, **7**, 500-512.
27. B. H. Kim, N. Lee, H. Kim, K. An, Y. I. Park, Y. Choi, K. Shin, Y. Lee, S. G. Kwon, H. B. Na, J. G. Park, T. Y. Ahn, Y. W. Kim, W. K. Moon, S. H. Choi and T. Hyeon, *J. Am. Chem. Soc.*, 2011, **133**, 12624-12631.
28. Z. Li, P. W. Yi, Q. Sun, H. Lei, H. L. Zhao, Z. H. Zhu, S. C. Smith, M. B. Lan and G. Q. Lu, *Adv. Funct. Mater.*, 2012, **22**, 2387-2393.
29. R. C. Atkins, *J. Chem. Educ.*, 1975, **52**, 550-550.
30. L. Shen, J. Bao, D. Wang, Y. Wang, Z. Chen, L. Ren, X. Zhou, X. Ke, M. Chen and A. Yang, *Nanoscale*, 2013, **5**, 2133-2141.
31. R. Costo, V. Bello, C. Robic, M. Port, J. F. Marco, M. P. Morales and S. Veintemillas-Verdaguer, *Langmuir*, 2012, **28**, 178-185.
32. X. M. Sun and Y. D. Li, *Angew. Chem. Int. Ed.*, 2004, **43**, 597-601.
33. A. Golon and N. Kuhnert, *J. Agric. Food Chem.*, 2012, **60**, 3266-3274.
34. S. Srivastava, R. Awasthi, D. Tripathi, M. K. Rai, V. Agarwal, V. Agrawal, N. S. Gajbhiye and R. K. Gupta, *Small*, 2012, **8**, 1099-1109.
35. Y. Hu, X. Gao, L. Yu, Y. Wang, J. Ning, S. Xu and X. W. Lou, *Angew. Chem. Int. Ed.*, 2013, **52**, 5636-5639.
36. M. Sevilla and A. B. Fuertes, *Chem. Eur. J.*, 2009, **15**, 4195-4203.
37. W. Jiang, X. Zhang, Z. Sun, Y. Fang, F. Li, K. Chen and C. Huang, *J. Magn. Magn. Mater.*, 2011, **323**, 2741-2747.
38. J. Muzart, *Tetrahedron*, 2009, **65**, 8313-8323.
39. F. Hu and Y. S. Zhao, *Nanoscale*, 2012, **4**, 6235-6243.
40. J. S. Ananta, B. Godin, R. Sethi, L. Moriggi, X. Liu, R. E. Serda, R. Krishnamurthy, R. Muthupillai, R. D. Bolskar, L. Helm, M. Ferrari, L. J. Wilson and P. Decuzzi, *Nat. Nanotechnol.*, 2010, **5**, 815-821.
41. P. Kucheryavy, J. He, V. T. John, P. Maharjan, L. Spinu, G. Z. Goloverda and V. L. Kolesnichenko, *Langmuir*, 2013, **29**, 710-716.
42. Z. Li, S. X. Wang, Q. Sun, Zhao,, H. L., H. Lei, M. B. Lan, Z. X. Cheng, X. L. Wang, S. X. Dou and G. Q. Lu, *Adv. Healthcare Mater.*, 2013, **2**, 958-964.
43. S. Laurent, D. Forge, M. Port, A. Roch, C. Robic, L. V. Elst and R. N. Muller, *Chem. Rev.*, 2008, **108**, 2064-2110.
44. L. J. Wang, Q. Wu, S. Tang, J. F. Zeng, R. R. Qiao, P. Zhao, Y. Zhang, F. Q. Hu and M. Y. Gao, *Rsc Adv.*, 2013, **3**, 23454-23460.
45. A. Roch, Y. Gossuin, R. N. Muller and P. Gillis, *J. Magn. Magn. Mater.*, 2005, **293**, 532-539.
46. J. Ward, J. A. Guthrie, D. J. Scott, J. Atchley, D. Wilson, M. H. Davies, J. I. Wyatt and P. J. Robinson, *Radiology*, 2000, **216**, 154-162.
47. F. Zhang, X. Huang, C. Qian, L. Zhu, N. Hida, G. Niu and X. Chen, *Biochem. Biophys. Res. Commun.*, 2012, **425**, 886-891.
48. H. S. Choi, W. Liu, P. Misra, E. Tanaka, J. P. Zimmer, B. I. Ipe, M. G. Bawendi and J. V. Frangioni, *Nat. Biotechnol.*, 2007, **25**, 1165-1170.
49. M. Longmire, P. L. Choyke and H. Kobayashi, *Nanomedicine*, 2008, **3**, 703-717.

Graphical and textual abstract for the contents pages

Facile non-hydrothermal synthesis of oligosaccharides coated sub-5 nm magnetic iron oxide nanoparticles with dual MRI contrast enhancement effect

Jing Huang,[a] Liya Wang,[a] Xiaodong Zhong,[b] Yuancheng Li,[a] Lily Yang,[c] Hui Mao [a]*

[a] Department of Radiology and Imaging Sciences, Emory University School of Medicine, Atlanta, Georgia 30322, USA.
[b] MR R&D Collaborations, Siemens Healthcare, Atlanta, Georgia 30322, USA.
[c] Department of Surgery, Emory University School of Medicine, Atlanta, Georgia 30322, USA.

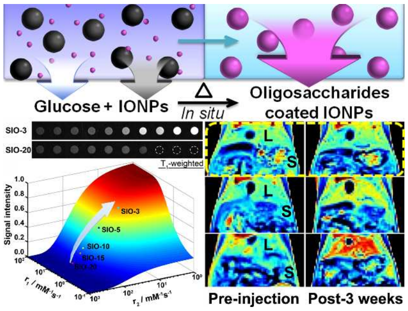

A simple non-hydrothermal method was developed for synthesizing sugar coated 3-nm magnetic nanoparticles with dual T_1-T_2 contrast enhancement and fast clearance.